Date of publication xxxx 00, 0000, date of current version xxxx 00, 0000.

Digital Object Identifier TBD.DOI

THz Cluster-Based Modeling and Propagation Characterization in a Data Center Environment

CHIA-LIN CHENG[1], (Student Member, IEEE), SEUN SANGODOYIN[1], (Member, IEEE), and ALENKA ZAJIĆ[1], (Senior Member, IEEE)

[1] School of Electrical and Computer Engineering, Georgia Institute of Technology, Atlanta, GA 30332 USA

Corresponding author: C.-L. Cheng (e-mail: cheng@gatech.edu)

This work has been supported, in part, by NSF grant 1651273. The views and findings in this paper are those of the authors and do not necessarily reflect the views of NSF.

ABSTRACT Terahertz (THz) wireless data centers can provide low-latency networks and dynamic scalability that are vital for the next-generation cloud computing infrastructure. The knowledge of THz propagation characteristics in a data center environment is essential to the development of novel THz communication systems. However, a comprehensive characterization and modeling of THz propagation channels, which includes various obstructions in a data center is not available. This paper presents results from a THz channel measurement campaign conducted in a data center environment. Various propagation scenarios such as line-of-sight (LoS) link, non-LoS (NLoS) link using existing materials in a data center to redirect the beam, and obstructed-LoS (OLoS), -NLoS (ONLoS) links with common objects in data centers (cables and server racks' mesh doors) serving as obstruction were investigated. Propagation channel parameters such as pathloss and root-mean-squared (RMS) delay spread were analyzed in the aforementioned scenarios while cluster-based modeling was implemented for some scenarios. The proposed model for THz propagation in a data center environment was validated with the measured data. The average inter-arrival time of clusters ($1/\Lambda$) and rays ($1/\lambda$) are estimated as 4.4 ns and 0.24 ns, respectively. We find that local scattering objects such as server-rack frames/pillars can be used to assist the NLoS type of link, and that cooling airflow in the data center has a negligible impact on THz propagation. Power cables and mesh doors of the server racks can cause additional attenuation of about 20 dB and 6 dB, respectively. Cluster model and other characterization results provided in this work are pertinent to THz wireless system design for data center environments.

INDEX TERMS Channel measurements, channel modeling, statistical channel model, terahertz (THz) communications, wireless data centers.

I. INTRODUCTION

CLOUD computing has become popular for on-demand computing services, such as storage and data processing. Increasing demand for cloud computing is driving the need for data centers that are equipped with low-latency networks and capable of dynamic scalability based on workloads [1], [2]. In traditional data centers, information exchange between servers mainly relies on wires and optical fiber cables. The use of the wires and cables increases the cost of assembly, maintenance, and operation, and service time [3]–[5]. Wired typologies impact the scalability and flexibility of the overall data center [6], [7]. Furthermore, cable bundles between server racks can block the cooling airflow and lead to inefficient cooling [8].

The use of a wireless (at Terahertz (THz) frequencies) approach in data centers would alleviate some of the aforementioned problems. The development of THz wireless system in data centers would require the characterization and modeling of the propagation channel in which such a device will operate. The data center environment is unique in its densely packed compartmentalized layout with rows of metallic server racks aligned in parallel and high performance computing servers with metal enclosures vertically stacked up in each rack. Exposed cable clusters, e.g., power cables, data cables, and auxiliary cables, exist between the server racks and server machines [3], [9]. This constitutes a unique propagation channel, whose properties need to be explored.

A. RELATED WORK

Several publications in the literature have explored the use of THz wireless links in data centers to achieve dynamic operation and higher reconfigurability [1], [10]–[14]. Moreover, THz frequencies promise a higher data rate with its large bandwidth and lower interference (due to the directional antennas) [15]–[20]. An IEEE 802.15.3d [21] standard for THz communication proposed a data rate of up to 100 Gbit/s at 252–325 GHz using eight different bandwidths between 2.16 GHz and 69.12 GHz. Simulation-based work in [12], [13] presented a stochastic channel model along with its simulation results for a THz wireless data center. However, measurement results were not provided. Measurement-based work in [14] presented a THz measurement campaign conducted in a data center. Results showed that path attenuation is comparable to Friis theoretical values and that THz wireless communication in a data center is possible. However, the measurement campaign did not investigate the propagation scenario with exposed cables serving as obstruction, which has been observed in some of the existing data centers [3], [9]. In our previous work [22]–[24], THz channel sounding measurements were conducted in a "data center-like" environment for the study of potential THz communication scenarios in a data center. The impacts of obstructions of cables, server racks, and their mesh structures on THz propagation were investigated, with corresponding channel properties developed. Moreover, propagation channel model for a blade-to-blade (B2B) link for the communication between vertically stacked servers was proposed. However, these prior measurements were not conducted in an actual data center but a mock-up model of a data center. In [25], amplitude fading statistics in a 4 × 4 MIMO channel were analyzed in a data center environment. However, the communication scenario is limited to short-range links with transmitter (Tx)-receiver (Rx) separation distance, d $<$ 40 cm.

B. CONTRIBUTION

As seen from the above literature survey, there is a lack of a comprehensive characterization and modeling of THz propagation channels that includes various obstructions in a data center. This paper attempts to fill this gap. We present details from the THz channel measurement campaign conducted in a data center environment with consideration for propagation scenarios including line-of-sight (LoS) link, non-LoS (NLoS) link using existing materials in a data center to redirect the beam, and obstructed-LoS (OLoS)/obstructed-NLoS (ONLoS) links. Optical lenses are used to extend the Tx-Rx separation distance in this work. We analyze propagation parameters such as pathloss and root-mean-square (RMS) delay spread in the aforementioned scenarios. The Tx/Rx misalignment tolerance range in the LoS link is also characterized. We test the possibility of using server-rack frames/pillars opposite to the transmitter as reflectors for the NLoS type of link and investigate the effect of cooling airflow on the THz propagation. The gain from the lenses and the attenuation caused by the power cables and server-rack mesh door are also characterized. We observed that multipath components (MPCs) naturally group into clusters in some of the measurements conducted. Therefore, a cluster-based propagation model for THz propagation in a data center environment has been proposed in such scenarios. Cluster-based models have been widely used for indoor propagation channels across a wide range of frequency spectra, from microwave (cellular), ultra-wideband (UWB), mm-wave, up to THz bands [26]–[35]. Clustering in the delay domain directly affects the delay spread, which is important in determining the need for employing channel protection techniques, e.g., channel equalization, channel coding, or channel diversity to overcome the dispersive effects of multipaths [36]. Regardless of such wide applicability and the aforementioned importance, no cluster-based model has been developed for THz propagation channels in data center environments. Our proposed clustering model is validated with measured data, and the corresponding inter- and intra-cluster parameters and their relevant statistics are presented in this work.

C. ORGANIZATION

The rest of the paper is organized as follows. The measurement campaign is described in Section II. Section III presents the characterization of pathloss, power delay profile (PDP), and delay spread, and introduces the proposed clustering model and the corresponding model validation. Concluding remarks are presented in Section IV.

II. MEASUREMENT CAMPAIGN

A. MEASUREMENT SETUP

A frequency-domain channel sounder setup was used for performing the experiment. At the heart of the measurement setup is a Keysight N5224A PNA vector network analyzer (VNA) and Virginia Diodes, Inc. (VDI) transceivers (Tx210/Rx148) [37], which operate over a bandwidth of 20 GHz (300–320 GHz) with 801 frequency tones. The THz carrier signal is generated from electronic sources using voltage-controlled oscillators and subsequent frequency multipliers. An input signal in the range of 10 MHz–20 GHz with a power level (P_{in}) of 0 dBm is generated by the VNA and fed into the VDI Tx210 (shown in Fig. 1 (a)). Inside the Tx210, a Herley-CTI phase-locked dielectric resonator oscillator (PDRO with 100 MHz reference crystal oscillator) [38] generates a 25 GHz signal, which is amplified and its frequency doubled using Norden N08-1975 [39], and then tripled by VDI WR6.5X3 [40]. This signal is then fed into a sub-harmonic mixer WR2.8SHM [41] that doubles the carrier frequency and mixes it with the baseband signal (10 MHz–20 GHz) generated from the VNA. The signal is then transmitted by the horn antenna in the THz range of 280–320 GHz. At the Rx (shown in Fig. 1 (b)), same components are used to down-convert the signal, except that the PDRO is tuned to 24.2 GHz, which leads to a down-conversion of the received signal to an intermediate frequency (IF) of 9.6 GHz. The upper sideband of the down-converted signal is then recorded by the VNA in the frequency range of 9.61–29.6 GHz. A block diagram of the measurement system and data processing procedure is shown in Fig. 1 (c), and the corresponding measurement parameters are summarized in Table 1.

TABLE 1. Measurement Parameters

Parameter	Symbol	Value
Measurement points	N	801
Intermediate frequency bandwidth	Δf_{IF}	20 kHz
Average noise floor	P_N	-90 dBm
Input signal power	P_{in}	0 dBm
Start frequency	f_{start}	10 MHz
Stop frequency	f_{stop}	20 GHz
Bandwidth	B	19.99 GHz
Time domain resolution	Δt	0.05 ns
Maximum excess delay	τ_m	20 ns

Vertically polarized pyramidal horn antennas [42] with gain that varies from 22 to 23 dBi from 300 to 312 GHz were used for this measurement campaign. The nominal half-power beamwidth (HPBW) of the horn antenna is about 10° in azimuth and elevation.

Plano-convex Polytetrafluoroethylene (PTFE/Teflon) lenses [43] with a focal length of 7.5 cm and a diameter of 5 cm are used to collimate the THz beam and provide extra gain for the scenarios in Sections II-B1–II-B4. The relative position of the lenses and the Tx/Rx are shown in Fig. 2 (a). Note that the distance between the horn and the lens is fixed at 6 cm.

Please note that we included the lenses as part of the channel rather than part of the measurement system, i.e., the gain of the lenses is included in the measurements, since channel characteristics such as multipaths have been identified as the results of reflections from the lenses. Additionally, the gain information of the PTFE optical lenses is not available.

B. MEASUREMENT ENVIRONMENT

The propagation channel measurements were conducted in a data center at the Tech Way Building on the campus of the Georgia Institute of Technology, Atlanta, GA. Inside the data center, high performance computing servers with metal enclosures are vertically stacked up in metallic server racks, and rows of server racks are arranged in parallel separated by aisles. Each server rack has a movable door with mesh structure that allows for circulation of the cooling airflow. Exposed cable clusters, e.g., power cables and auxiliary cables are observed among the server racks.

In our measurement campaign, five wireless data center scenarios have been considered: 1) LoS link, where a server from one rack communicates to the server in the next-aisle rack; 2) OLoS link, where the LoS link is obstructed by common objects in data centers, such as cables and server racks' mesh doors; 3) NLoS link, where servers in adjacent racks communicate with each other through reflections of the server-rack frames/pillars in the next aisle; 4) ONLoS link, where the NLoS link is obstructed by server racks' mesh doors; 5) Tx and Rx are placed at the opening of the cooling grille on the floor to study the effects of cooling airflow on THz propagation.

1) LoS Link

We envision that THz transceivers and optical lenses will eventually be integrated into the server chassis such that THz links can be established for server-to-server communications. Our measurement setup for the LoS link is presented in Fig. 3, where the Tx is placed in the server cabinet on the left side of the aisle and the Rx is placed in the server cabinet on the right side of the aisle with a Tx-Rx separation distance, d = 175 cm. We have also tested a scenario where misalignment exists between the Tx and Rx. In reality, each server rack may be configured for different applications using different types of servers with different heights [44]. In such case, the Tx and Rx that are integrated into the server enclosure may not be perfectly aligned in the vertical direction. Therefore, an investigation of the tolerance range of the vertical offset between the Tx and Rx is in order. A schematic of the measurement setup for the LoS link with vertical offset is presented in Fig. 2 (b), where the vertical offset range, h, varies from 0 to 6 cm with a step size of 1 cm.

Note that several possible LoS propagation links in wireless data centers were presented in [12, Sec. II, para. 3], [14, Sec. II-B, para. 1, and Sec. II-C, para. 1], [45, Sec. II, para. 1], including links with Tx/Rx placed on top of the rack (ToR) and on the lower level of the rack. In our LoS setup, we investigate the case with Tx/Rx placed on the lower level of the rack since the ToR link has already been studied in [14, Sec. IV, para. 1], with measurement results showing a path attenuation, which followed the Friis propagation model. Moreover, according to [12, Sec. II, para. 4], by placing Tx/Rx on the lower level of the rack, interference [45, Sec. II, para. 4] from the ToR link can be avoided.

2) OLoS Link

Next, we investigate the OLoS scenario where the wireless channel is obstructed by objects commonly found in data centers such as cables and mesh doors. We envision that THz transceivers and optical lenses will be integrated into the server chassis, which implies that the mesh door on the server rack may obstruct the LoS link between the Tx and Rx. Therefore, we evaluate the impact of mesh door on THz links. For the OLoS link with mesh door serving as obstruction, measurements were recorded at d = 175 cm with the mesh door on the Tx rack (left side in Fig. 3) closed, while the mesh door on the Rx rack (right side in Fig. 3) stayed open. A focused view of the mesh structure is shown

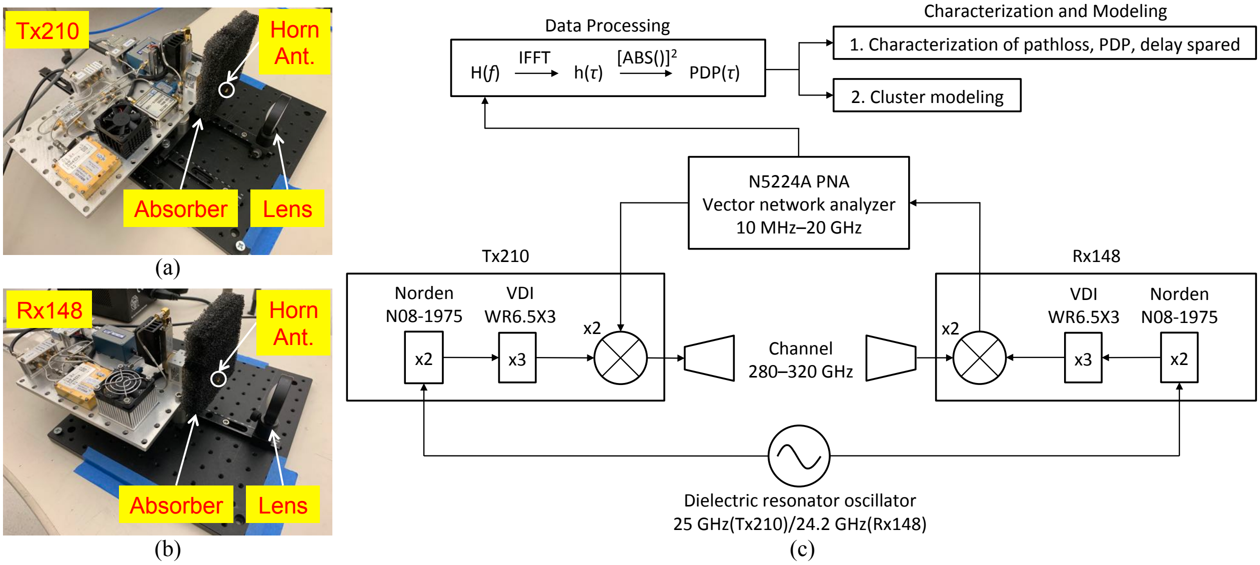

FIGURE 1. (a) Tx and (b) Rx configurations, (c) block diagram of the measurement system and data processing procedures.

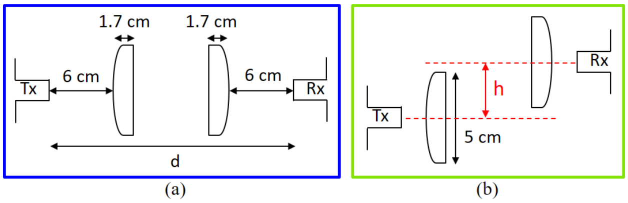

FIGURE 2. (a) Plano-convex PTFE lens configuration; (b) illustration of the LoS vertical offset measurement setup, where h varies from 0 to 6 cm with a step size of 1 cm.

FIGURE 3. Measurement setup for the LoS link at d = 175 cm.

in Fig. 4 (a). It is important to note that with the wired data links in existing data centers replaced with wireless links, the remaining power cables may serve as obstruction and interfere with the wireless propagation channels. Therefore, we intended to study the OLoS scenario with power cables serving as obstruction. Fig. 4 (b) presents the existing power cables in a data center that we used for the OLoS scenario. It can be observed in Fig. 4 (b) that existing power cables in data centers are distributed nonuniformly, with some parts consisting of multiple cables fastened together, which create a thicker cable cluster (e.g., orange cable clusters in Fig. 4 (b)); while some other parts are formed by individual cable, which lead to a thinner and scattered cable cluster (e.g., blue and yellow cable clusters in Fig. 4 (b)). Such nonuniformly composed cable clusters create obstructions with varying thickness sizes and can cause fading in THz propagation channels. In order to obtain a generalized statistical evaluation of the fading caused by cables with various thickness sizes, we recorded the measurements as Tx and Rx are placed at 26 different horizontal positions with a step size of 0.5 cm and d = 175 cm to ensure that the interaction between THz waves and different parts of the cable clusters can be captured. An illustration of the measurement setup is presented in Fig. 5. Note that the number of Tx/Rx horizontal positions could not exceed 26 due to limited space in the server rack compartment.

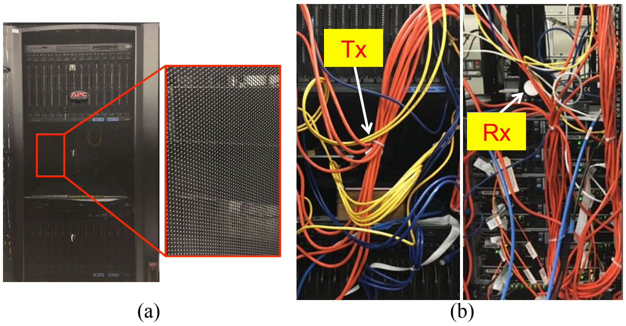

FIGURE 4. (a) Mesh structure on a server rack door and (b) the cable clusters at the Tx and Rx.

3) NLoS Link

In the NLoS link, reflectors were used to redirect the the transmitted signal in order to bypass obstructions and aid transmission [5]. Previous works [7], [12], [45], [46] suggested covering the ceiling in the server room with reflective

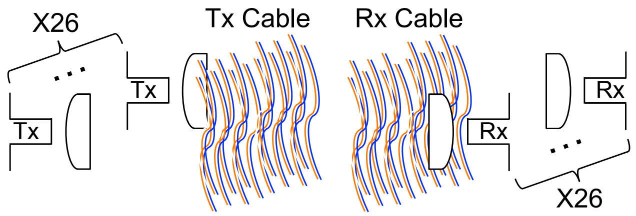

FIGURE 5. Illustration of the OLoS link with cables serving as obstruction. The step size between each Tx/Rx position is 0.5 cm.

materials thereby using it as a reflector for the NLoS type of link. This approach increases cost and takes up a considerable amount of space. As an alternative, we propose the possibility of using existing objects in a data center as reflectors for the NLoS link. Our setup for the NLoS link is presented in Figs. 6 (a) and (b), where the server-rack frame/pillar of the server rack is used as the reflector. Measurements were recorded at a path length of 282 cm.

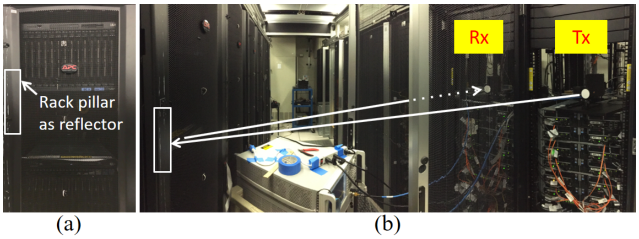

FIGURE 6. (a) The server-rack frame/pillar that is used as a reflector; (b) measurement setup for the NLoS link at a path length of 282 cm.

4) ONLoS Link

The ONLoS scenario was also investigated, where the NLoS link introduced in Section II-B3 is obstructed by the mesh door on the server rack. Similar to the setup in Fig. 6 (b), here we close the mesh door on the Tx rack while leave the mesh door on the Rx rack open. Measurements were recorded at a path length of 282 cm.

5) Effects of Cooling Airflow on THz Propagation

THz propagation encounters frequency- and moisture-dependent amplitude variation due to the molecular absorption (mainly related to an outdoor environment) at the THz bands [47]. In a data center, strong airflow from the cooling grille creates abrupt motion change to the movement of the air molecules. We investigate the cooling airflow effect on THz propagation due to the abrupt molecular movement around the cooling grille. Fig. 7 (a) presents the top-down view of the cooling grille used for our measurements. Figs. 7 (b) and (c) show the side-view of our measurement setup with cooling airflow passing through the grille and being blocked, respectively. The zero-span mode (single-frequency mode runs over time) in the VNA was used to record signal amplitude variation over time at 300 GHz with d = 9 cm. We use a 30 cm (width) x 15 cm (length) styrofoam board to block the airflow. To verify whether the airflow was really blocked by the styrofoam board, we held a piece of tissue paper on top of the styrofoam board and used visual inspection to examine whether the tissue paper was moved by the airflow. The tissue paper was observed to be stationary, and thus confirmed that the styrofoam board effectively blocked the airflow. Note that in order to have a fair comparison, we made sure that during the transition between setups in Figs. 7 (b) and (c), only the styrofoam board that blocked the airflow was moved while the Tx/Rx alignment remained unchanged.

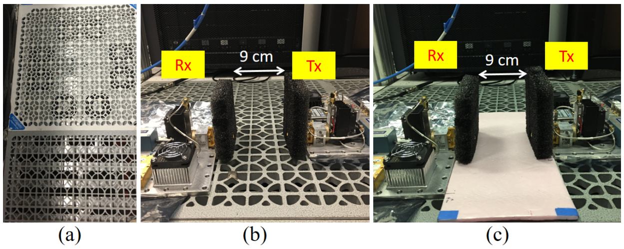

FIGURE 7. (a) Top-down view of the cooling grille in a data center; side-view of the measurement setup with cooling airflow (b) passing through and (c) being blocked.

III. MEASUREMENT ANALYSIS AND RESULTS

This section presents the measurement analysis and the corresponding results of the following studies: 1) characterization of pathloss, PDP, and root-mean-square (RMS) delay spread; 2) cluster-based modeling of PDP.

A. CHARACTERIZATION OF PATHLOSS, PDP, AND DELAY SPREAD

In our analysis, the mean pathloss ($\overline{PL}$) is calculated by averaging the magnitude squared of the channel transfer function over an ensemble of frequency tones,

$$\overline{PL} = \frac{1}{N}\sum_{i=1}^{N} |H(f_i)|^2, \tag{1}$$

where $N = 801$ is the number of frequency tones and $H(f_i)$ is the measured channel transfer function. We obtain the channel impulse response by performing the inverse discrete Fourier transform (IDFT) over the measured channel frequency response. RMS delay spread (τ_{rms}) is estimated by the calculation of the square root of the second central moment of the normalized squared magnitude of the channel impulse response [48, (11.8)], i.e.,

$$\tau_{rms} = \sqrt{\frac{\sum\limits_{k=1}^{L} |h(\tau_k)|^2 \tau_k^2}{\sum\limits_{k=1}^{L} |h(\tau_k)|^2} - \tau_m^2}, \tag{2}$$

where τ_k is the excess delay of the k^{th} path relative to the first arrival, $|h(\tau_k)|^2$ is the PDP, L is the number of MPCs, and τ_m is the mean excess delay defined as

$$\tau_m = \frac{\sum_{k=1}^{L} |h(\tau_k)|^2 \tau_k}{\sum_{k=1}^{L} |h(\tau_k)|^2}. \tag{3}$$

1) **LoS Link Analysis**

In this section, we characterize pathloss, PDP, and τ_{rms} in the LoS scenario as introduced in Fig. 3 in Section II-B1.

The empirical and analytical (from Friis equation) pathloss results have been provided in Fig. 8. By comparing the Friis pathloss curve (black dash line with average loss = 87 dB) and the measured LoS pathloss curve (red diamond with average loss = 57.7 dB), we find that the optical lens does provide an additional gain of around 29.3 dB by focusing the THz signal. A representation of the measured PDP has been provided in Fig. 9. Three distinct multipath components observed in this type of scenario have been labeled in the plot. The origins of these multipath components are subsequently discussed. MPC1 results from the sum of reflections between the lens and the horn at both Tx and Rx, where reflection at each end has a time delay of 0.4 ns. The sum of time delay at both Tx and Rx results in a total time delay of 0.8 ns. For the reflections between the lens and the horn at either Tx or Rx, the corresponding MPC is observed as unresolvable congested spikes at 0.4 ns (highlighted in blue circle in Fig. 9) due to limited temporal resolution. MPC2 results from reflections between Tx lens and Rx horn and between Rx lens and Tx horn. To be more specific, MPC2 has a delay about 11.4 ns corresponding to an additional delay path of 342 cm that is twice the distance from the Rx horn to the Tx lens plus multiple reflected paths within the Rx lens. MPC3 is due to Rx horn-to-Tx horn reflection. To be more specific, MPC3 has a delay around 12 ns corresponding to an additional delay path of 360 cm that is twice the distance from the Tx horn to the Rx horn plus multiple reflected paths within the Tx and Rx lenses. Since the area surrounding the Tx and Rx horns are covered with absorbers as shown in Figs. 1 (a) and (b), we can infer that the internal surfaces and the tips of the horns are the cause of horn-related reflections. The corresponding τ_{rms} in the LoS link is estimated as 0.295 ns. For the ease of reference, measured mean pathloss and τ_{rms} in the LoS link are summarized in the first row in Table 2.

TABLE 2. Measured Mean Pathloss and τ_{rms}

Scenario		Distance	Pathloss	τ_{rms}
LoS	Door open	175 cm	57.7 dB	0.295 ns
OLoS	Door closed		63.4 dB	0.113 ns
NLoS	Door open	282 cm	78.4 dB	0.372 ns
ONLoS	Door closed		84.4 dB	0.299 ns

Next, the LoS scenario with vertical offset between the Tx and Rx was investigated. The setup used for this measurement has been illustrated in Fig. 2 (b), where the vertical offset range, h, varies from 0 to 6 cm with a step size of 1 cm. Fig. 10 shows the measured pathloss over frequency with various Tx-Rx offset values. It can be observed that as the offset approaches 6 cm, the pathloss value gradually increases and the fluctuation becomes more prominent. The pathloss fluctuation results from the fact that the received signal is approaching the noise floor. Note that when offset exceeds 6 cm, there is no signal reception but only noise floor observed. Similar observation of the pathloss fluctuation in the THz bands can be found in [16]. Fig. 11 presents the measured mean pathloss (red solid line) and the measured τ_{rms} (black dash line) with respect to Tx-Rx offset values. It can be observed in the offset range of 0–4 cm, the measured mean pathloss has an increment of 6.1 dB from 57.7 dB to 63.8 dB, while in the offset range of 4–6 cm, the pathloss has a more rapid increment of 23.6 dB from 63.8 dB to 87.4 dB. The τ_{rms} varies between 0.12–0.3 ns in the offset range of 0–4 cm, and 0.15–1 ns in the offset range of 4–6 cm, respectively. Coincidentally, the breakpoint around 4 cm

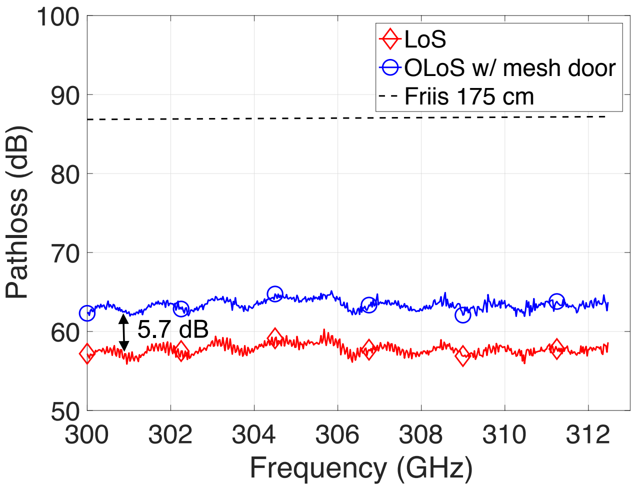

FIGURE 8. Measured pathloss in the LoS (red diamond) and OLoS (blue circle) links at d = 175 cm along with Friis pathloss (black dash line) at d = 175 cm.

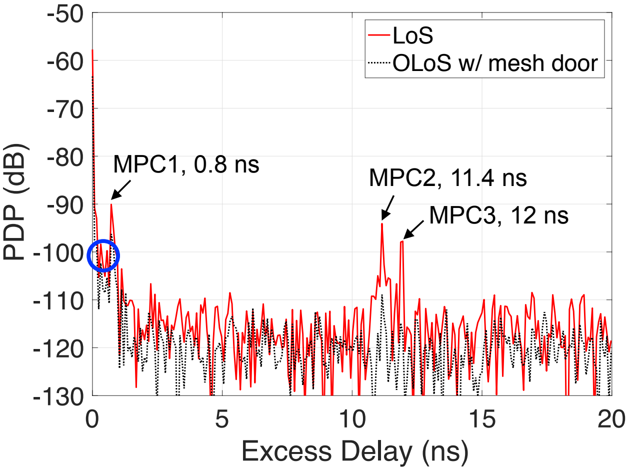

FIGURE 9. Measured PDP in the LoS (red solid line) and OLoS (black dot line) links at d = 175 cm.

approximates the lens diameter of 5 cm, which is reasonable since discontinuity of propagation channel properties can be expected when the Tx-Rx misalignment exceeds the aperture size. As a result, more abrupt change in the pathloss and τ_{rms} should be considered when the Tx-Rx misalignment approaches the boundary of the lens. Note that if we look into the τ_{rms} curve in Fig. 11 during the offset distance of 0–4 cm, we can find that τ_{rms} first decreases about 0.2 ns during offset range of 0–2 cm, and then starts to increase during offset range of 2–4 cm. This is because during offset range of 0–2 cm, multipaths mainly come from the reflections between the lenses and horn antennas as explained in the previous paragraph. As offset increases from 0 cm, the aforementioned reflections start to attenuate due to the Tx/Rx misalignment, and thus result in decreased τ_{rms}. In the offset range of 2–4 cm, reflection from the surrounding environment (e.g., server enclosures and rack compartments) leads to a wider MPC as shown in Fig. 12 and thus slightly increases the τ_{rms}. As offset distance increases beyond 4 cm, the main cause of rapid increase in the τ_{rms} is dominated by the attenuation of the first arrival path, which causes τ_{rms} to increase according to (2).

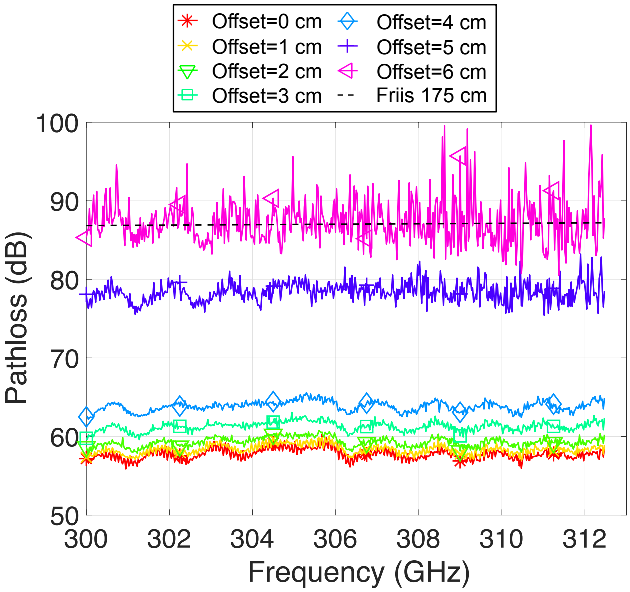

FIGURE 10. Measured pathloss and Friis pathloss (black dash line) in the LoS link at d = 175 cm with Tx-Rx vertical offset varying from 0 to 6 cm.

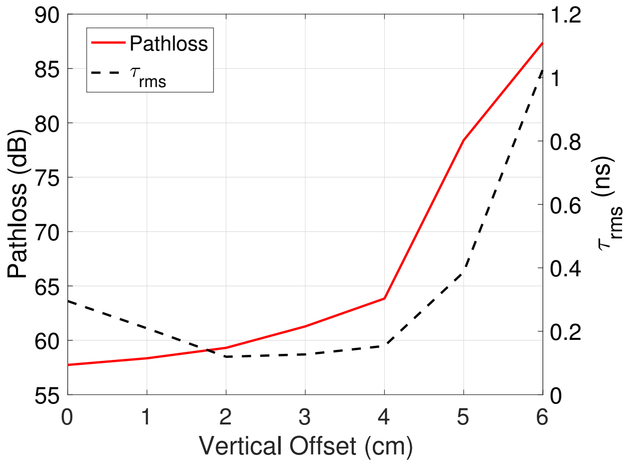

FIGURE 11. Measured mean pathloss (red solid line) and measured τ_{rms} (black dash line) versus Tx-Rx offset values in the LoS link at d = 175 cm.

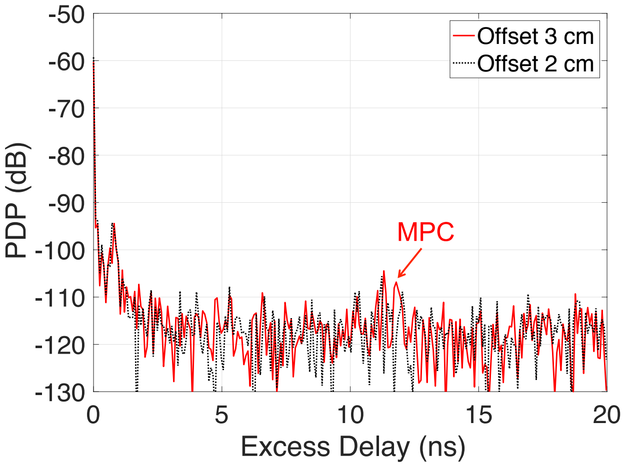

FIGURE 12. Measured PDP in the LoS link at d = 175 cm with Tx-Rx vertical offset of 2 cm (black dash line) and 3 cm (red solid line).

2) OLoS Link Analysis

In this section, we characterize the pathloss, PDP, and τ_{rms} in the OLoS scenario as introduced in Section II-B2.

Figure 8 (blue circle) shows the measured pathloss in the OLoS link with mesh door serving as an obstruction. The measured mean pathloss is calculated as 63.4 dB. By comparing the mean pathloss in the LoS link and OLoS link, we can conclude that the additional loss resulting from the mesh door is around 5.7 dB. Fig. 9 shows the measured PDP in the OLoS link, with the corresponding τ_{rms} estimated as 0.113 ns. Interestingly, the PDP showed that with the obstruction of mesh door, multipaths are significantly attenuated compared to the LoS link, and that the τ_{rms} is reduced from 0.295 ns to 0.113 ns. For the ease of reference, measured mean pathloss and τ_{rms} in the OLoS link with mesh door serving as obstruction are summarized in the second row in Table 2.

As explained in Section II-B2, cable clusters used in the OLoS link are distributed nonuniformly with irregular shapes and various thickness sizes. This cable composition in the OLoS propagation channel can eventually lead to small-scale fading. Figs. 13 and 14 present the measured pathloss and PDP in the OLoS link with cables serving as obstruction, where variations in pathloss and multipath distribution (highlighted in Fig. 14) that are dependent on the Tx/Rx horizontal positions with respect to the cable clusters were observed. We also performed a detailed statistical analysis over measurements from all the Tx/Rx horizontal positions. The corresponding statistics of the fading and the delay spread variation in the OLoS link with cables serving as obstruction are presented in Section III-B.

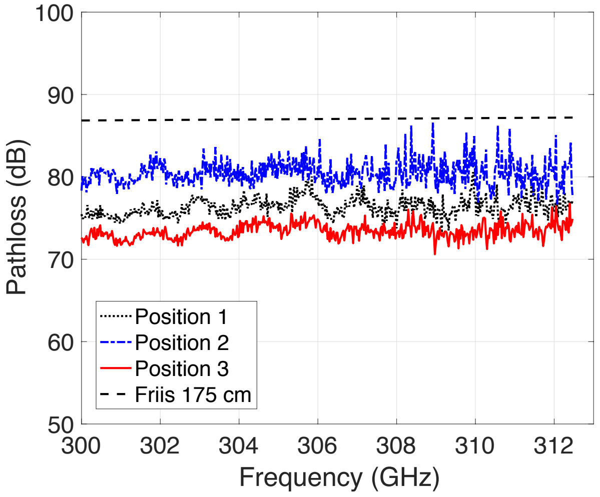

FIGURE 13. Measured pathloss and Friis pathloss (black dash line) in the OLoS link at d = 175 cm with cables serving as obstruction.

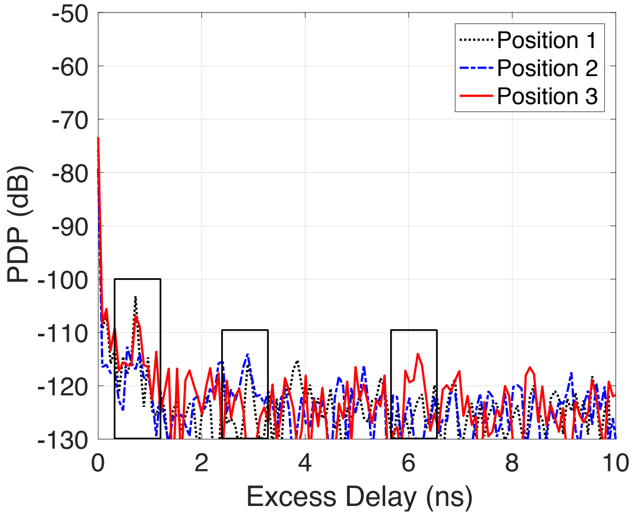

FIGURE 14. Measured PDP in the OLoS link at d = 175 cm with cables serving as obstruction.

3) NLoS Link Analysis

In this section, we analyze the pathloss, PDP, and τ_{rms} in the NLoS link as introduced in Fig. 6 in Section II-B3.

Figure 15 (red diamond) presents the measured pathloss in the NLoS link with server-rack frames/pillars serving as reflector. We found that the measured mean pathloss (averaged over all frequencies), 78.4 dB, is 12.6 dB lower than the mean Friis pathloss (averaged over all frequencies), 91 dB, at a path length of 282 cm. Therefore, we conclude that in the absence of a LOS link between Tx and Rx, an alternate mean of transmission would be to use local scatterers (such as the server-rack frames/pillars) as reflectors to aid transmission between Tx and Rx. Figure 16 (red solid line) shows the measured PDP in the NLoS link, where two distinctive MPCs were observed as labeled. MPC1 results from reflections between Tx lens and Tx horn and between Rx lens and Rx horn, where a time delay of 0.8 ns corresponds to four times of lens-to-horn distance. Note that the MPC1 in the NLoS link has similar delay as the MPC1 in the LoS link shown in Fig. 9 (red curve), while the amplitude of NLoS link's MPC1 is weaker due to longer propagation path. MPC2 results from reflections between the server-rack frame/pillar and the rack door that lies between the Tx and Rx. To be more specific, MPC2 has a delay about 6.7 ns corresponding to an additional delay path of 200 cm, which is twice the distance from the rack server-rack frame/pillar to the rack door. This result points out that although the server-rack frame/pillar can serve as an ideal reflector, it may also create additional scattered beams in the surrounding space and cause additional multipaths. The corresponding τ_{rms} in the NLoS link is estimated as 0.372 ns. For the ease of reference, measured mean pathloss and τ_{rms} in the NLoS link are summarized in the third row in Table 2.

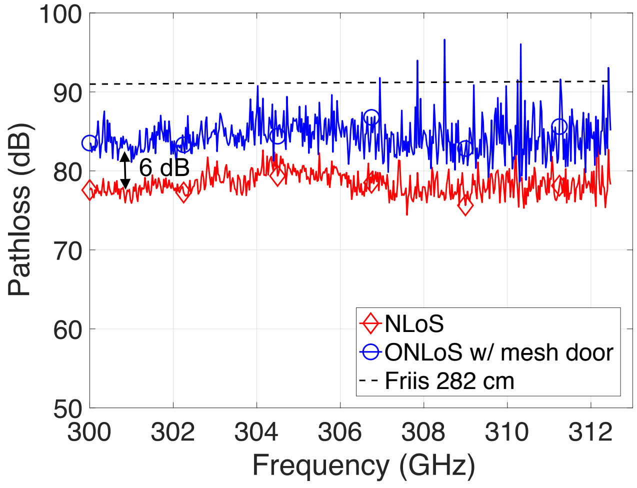

FIGURE 15. Measured pathloss in the NLoS (red diamond) and ONLoS (blue circle) links along with Friis pathloss (black dash line) at a path length of 282 cm.

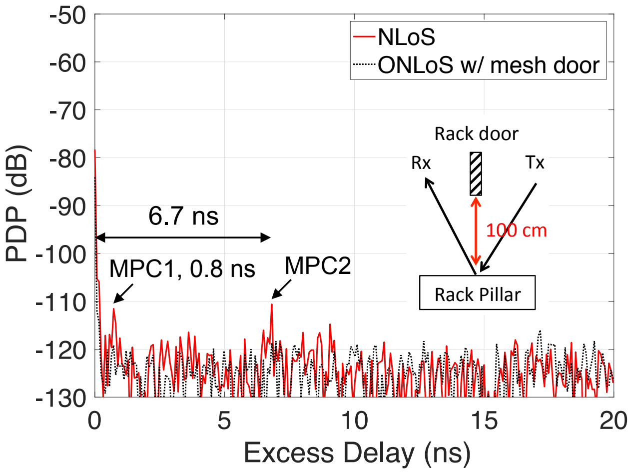

FIGURE 16. Measured PDP in the NLoS (red solid line) and ONLoS (black dot line) links at a path length of 282 cm.

4) ONLoS Link Analysis

In this section, we characterize the pathloss, PDP, and τ_{rms} in the ONLoS scenario as introduced in Section II-B4.

In Fig. 15, the measured pathloss in the ONLoS link with mesh door serving as obstruction, where the mean pathloss is estimated as 84.4 dB, has been presented. By comparing the mean pathloss in the NLoS link and ONLoS link, we have found that the additional loss resulting from the mesh door is around 6 dB, which is similar to the result in Section III-A2. Fig. 16 shows the measured PDP in the ONLoS link. Similar to the result in Section III-A2, MPCs are found to be attenuated by the obstruction of mesh door. Compared to the NLoS link, the τ_{rms} in the ONLoS link is reduced from 0.372 ns to 0.299 ns. For the ease of reference, measured mean pathloss and τ_{rms} in the ONLoS link are summarized in the fourth row in Table 2.

5) Effects of Cooling Airflow on THz Propagation

In this section, we investigate the impact of cooling airflow on THz propagation as introduced in Section II-B5. Fig. 17 presents the time domain measurement results using a 300 GHz carrier frequency with Tx-Rx separation distance of 9 cm. The average (ensemble over time) magnitude of the transfer function of the channel with (blue circle) and without (red diamond) cooling airflow is -51.61 dB and -51.63 dB, respectively, with a 0.02 dB difference. As a result, we conclude that the impact from the cooling airflow is negligible. Note that the lens wasn't used for this measurement due to a short Tx-Rx distance as shown in Fig. 7.

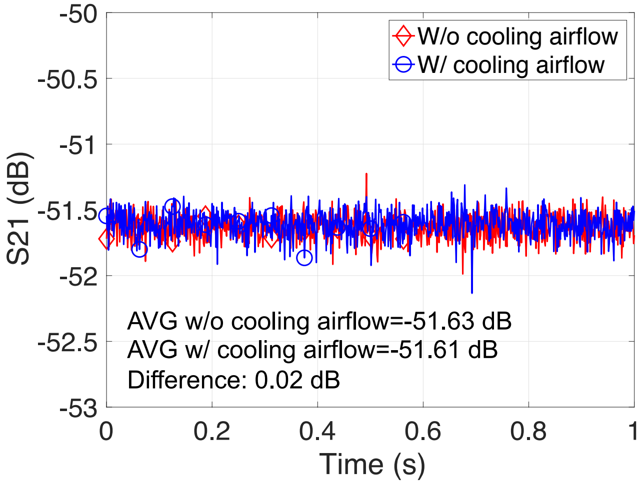

FIGURE 17. Magnitude of the transfer function of the channel with cooling airflow passing through (blue circle) and being blocked (red diamond). Measurements were recorded over time at 300 GHz at d = 9 cm.

B. CLUSTER-BASED MODELING OF PDP

In this section, we introduce a cluster-based channel model that can handle THz propagation in a data center environment with the use of optical lenses. We define a cluster as a group of MPCs having similar properties such as delays. Clusters primarily stem from interacting objects (or scatterers) such as obstructing cables, metallic shelves and doors in the data center environment. We use the K-power means clustering algorithm [31], [49] along with visual inspection [50]–[52] to obtain a reasonable number of clusters. Relevant channel statistics derived from the clustering model are discussed, and model validation is presented.

1) Proposed Clustering Model

The proposed clustering model in this work is based on a modified version of the widely-used Saleh-Valenzuela (S-V) model [26]. The assumption of the S-V model for the PDP is that MPCs arrive within several distinctly recognizable clusters. The PDP of the S-V model in dB can be expressed as [53],

$$PDP(\tau) = \sum_{l=1}^{L}\sum_{k=1}^{K_l}\Bigg[10\log_{10}\overline{\beta_{11}^2} - \overbrace{\frac{T_l}{\Gamma}(10\log_{10}e)}^{P(T_l)} - \overbrace{\frac{\tau_{kl}}{\gamma}(10\log_{10}e)}^{P(\tau_{kl})}\Bigg]\cdot\delta(\tau - T_l - \tau_{kl}), \tag{4}$$

where L is the number of clusters, K_l is the number of rays (MPCs) in the l^{th} cluster, $\overline{\beta_{11}^2}$ is the local mean power of the 1^{st} ray ($k = 1$) in the 1^{st} cluster ($l = 1$). T_l is the time of arrival of the l^{th} cluster, τ_{kl} is the delay of the k^{th} component relative to the time T_l, and $\delta(\cdot)$ denotes the Dirac delta function. Γ and γ are the cluster power and ray power decay rates, respectively.

Contrary to the traditional S-V model's assumption, we have found that Γ could not precisely capture the attenuation of the multipath clusters in the THz data center environment. Therefore, we propose a modified clustering model with Γ that is expressed into two sections as a function of delay,

$$\Gamma(\tau) = \begin{cases} \Gamma_1 & , 0 < \tau < \tau_{th}, \\ \Gamma_2 & , \tau_{th} \leq \tau < \tau_{Max}, \end{cases} \tag{5}$$

where τ_{th} is a delay threshold value serving as a breakpoint for Γ and can be selected based on the distribution of multipath clusters. Γ_1 and Γ_2 can be determined through linear regression of cluster peak powers in dB and the associated delays in nanoseconds. The ray power decay rate γ in each cluster can be obtained by

$$\gamma(\tau) = a\cdot\tau + b, \tag{6}$$

where $\gamma(\tau)$ and its parameters a and b can be determined through linear regression of intra-cluster powers in dB and the associated delays in nanoseconds. The S-V model assumes that the distributions of the cluster and ray arrival times may be described by stochastic Poisson processes, which implies that the distribution of inter-arrival time of clusters ($T_l - T_{l-1}$) can be described by independent exponential probability density function (PDF) as follows

$$p(T_l|T_{l-1}) = \Lambda \cdot e^{-\Lambda(T_l - T_{l-1})}, l > 0, \tag{7}$$

where Λ is the mean cluster arrival rate, and that the distribution of inter-arrival time of rays ($\tau_{kl} - \tau_{(k-1)l}$) can be expressed by the following PDF

$$p(\tau_{kl}|\tau_{(k-1)l}) = \lambda \cdot e^{-\lambda(\tau_{kl} - \tau_{(k-1)l})}, k > 0, \tag{8}$$

where λ is the mean ray arrival rate. A schematic illustration of the proposed S-V model introduced in (4)–(6) is shown in Fig. 18.

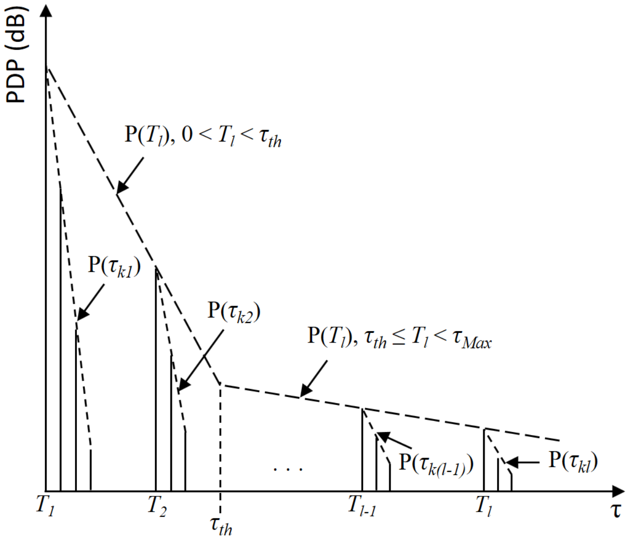

FIGURE 18. Schematic illustration of the proposed clustering model introduced in (4)–(6).

Figure 19 presents the normalized measured cluster power with respect to excess delay (τ), where the measured data are collected from an ensemble of all the measured positions from the OLoS, NLoS, and ONLoS scenarios as introduced in Section II-B. The black circles in Fig. 19 represent the normalized measured cluster peak powers from all the measured positions, where the normalization is with respect to the first arriving signal at each measured position. Solid red and dash-dot blue lines represent the linear regression fits of cluster peak powers with slopes (cluster power decay rates) of Γ_1 = -72.3 dB/ns and Γ_2 = -0.58 dB/ns, respectively, where the two regression lines intersect at an excess delay of τ_{th} = 0.7 ns. Parameters a, b for the ray power decay coefficient in (6) have been estimated as 5.48 dB/ns and -75.93 dB, respectively. The average inter-arrival time of clusters ($1/\Lambda$) and rays ($1/\lambda$) are estimated as 4.4 ns and 0.24 ns, respectively. In an ensemble of measured positions, the number of clusters is found to follow Poisson distribution with a mean of 3, while the number of rays is found to follow Rayleigh distribution with a mean of 4. For the ease of reference, parameters used in the proposed clustering model are summarized in Table 3.

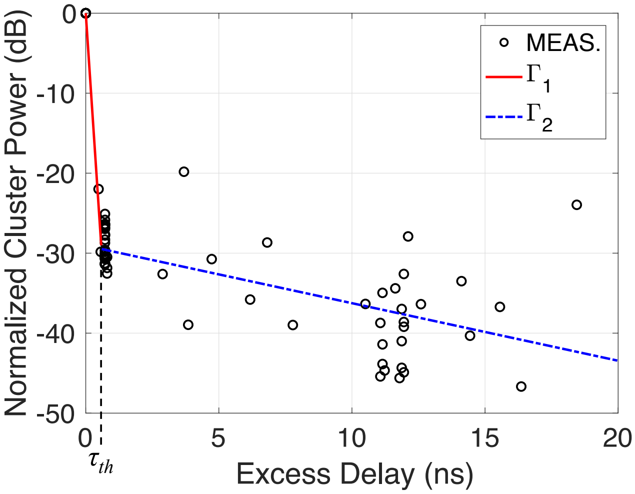

FIGURE 19. Normalized measured cluster power (black circles) versus excess delay (τ) and the corresponding linear regression fits with slopes of Γ_1 (red solid line) and Γ_2 (blue dot dash line).

TABLE 3. Clustering Model Parameters

Parameter	Value
τ_{th} (ns)	0.7
Γ_1 (dB/ns)	-72.3
Γ_2 (dB/ns)	-0.58
a (dB/ns)	5.48
b (dB)	-75.93
1/Λ (ns)	4.4
1/λ (ns)	0.24
Cluster No.	3
Ray No.	4

An example of the measured PDP from one of the measured positions in the OLoS scenario with cables serving as obstruction is shown in Fig. 20. It is observed that four clusters (highlighted by thick red lines) were clearly identified using the aforementioned approach. Note that the red lines in Fig. 20 are for annotation, not the actual model. Cluster 2 in Fig. 20 results from the reflections between the Tx lens and the Tx horn and between the Rx lens and the Rx horn. Clusters 3 and 4 consist of the scattered and reflected waves from the Tx/Rx cables. To be more specific, the peak power of cluster 3 is located at excess delay, τ = 11.8 ns, corresponding to an additional delay path of 354 cm that is twice the distance from the Tx horn to the Rx horn plus twice the distance between the Tx cable and the Tx lens and between the Rx cable and the Rx lens (the Tx/Rx cables are positioned at 8–10 cm in front of the Tx/Rx lenses). Within cluster 3, the peak power is followed by several MPCs that are 0.56 ns and 1.04 ns away. These MPCs are the results of the single-bounced and double-bounced reflections between the Tx/Rx cables and the Tx/Rx lenses, since the delays of 0.56 ns and 1.04 ns are two times and four times of the distance between the Tx/Rx cables and the Tx/Rx lenses, respectively. The peak power of cluster 4 is located at τ = 16.4 ns, corresponding to an additional delay path of 492 cm

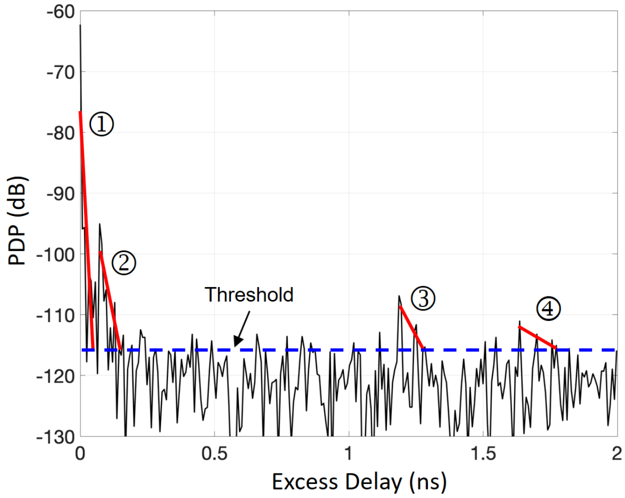

FIGURE 20. Measured PDP and the identified clusters in the OLoS link with cables serving as obstruction.

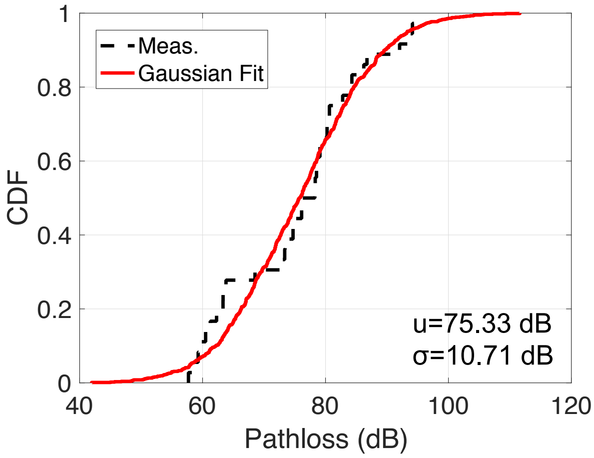

FIGURE 21. CDF of the mean pathloss measured from all the measured positions in the OLoS, NLoS, and ONLoS links.

that is twice the distance between the Tx cables and Rx cables plus twice the distance between the Tx cable and the Tx lens and between the Rx cable and the Rx lens. Within cluster 4, the peak power is followed by several MPCs that are 0.64 ns and 1.2 ns away. Similar to the observation in cluster 3, these MPCs are the results of the single-bounced and double-bounced reflections between the Tx/Rx cables and the Tx/Rx lenses, since the delays of 0.64 ns and 1.2 ns are two times and four times of the distance between the Tx/Rx cables and the Tx/Rx lenses, respectively. In contrast to cluster 3, the MPCs in cluster 4 decay at a slower rate due to longer propagation path. Note that for all the measured PDPs, the excess delay (τ) of the first arriving MPC is normalized to 0 ns. Noise filtering was performed on PDPs by setting a threshold level of 8 dB above the noise floor as shown in Fig. 20. PDP values below this threshold are considered as noise and equaled to zero.

2) Pathloss and Shadowing

In this section, we analyze the pathloss and the shadowing gain using an ensemble of all measured positions from the OLoS, NLoS, and ONLoS scenarios. We found that the logarithmic equivalent of the pathloss can be modeled as Gaussian distribution, with mean value (μ (dB)) of 75.33 dB and a standard deviation (σ) of 10.71 dB, which corresponds to the bulk shadowing gain. The cumulative distribution function (CDF) of the aforementioned pathloss is presented in Fig. 21.

3) Clustering Statistics

This section analyzes the statistics of the clustering model derived in Section III-B1, such as cluster shadowing, distributions of the number of clusters and rays, and correlation coefficient matrix of relevant channel parameters.

The cluster shadowing gain is defined as the difference between the measured cluster power and the expected value that is estimated from the cluster power decay constant ($\Gamma(\tau)$ in (5)). The cluster shadowing gain in our analysis is modeled to be log-normally distributed, where its value in dB approximates a zero-mean Gaussian distribution with $\sigma = 7.95$ dB. The PDF of the cluster shadowing gain derived from the clustering model is shown in Fig. 22. The fitness of the distribution with respect to the measured data has been quantified by a maximum deviation value metric [54], $D_v = \mathrm{Max}|F_{\text{measurement}}(\mathrm{x}) - F_{\text{test}}(\mathrm{x})|$, where $F_{\text{measurement}}(\mathrm{x})$ and $F_{\text{test}}(\mathrm{x})$ are the CDFs of the measured cluster shadowing gain and the tested distributions, respectively. Several typical theoretical distributions such as log-normal, Rayleigh, exponential, Nakagami, normal, Rician, and Weibull have been tested, and the results are shown in the second column in Table 4. The log-normal distribution is found to have the smallest D_v of 0.057 among all the tested distributions, which is small according to [55] and thus confirms a good fit.

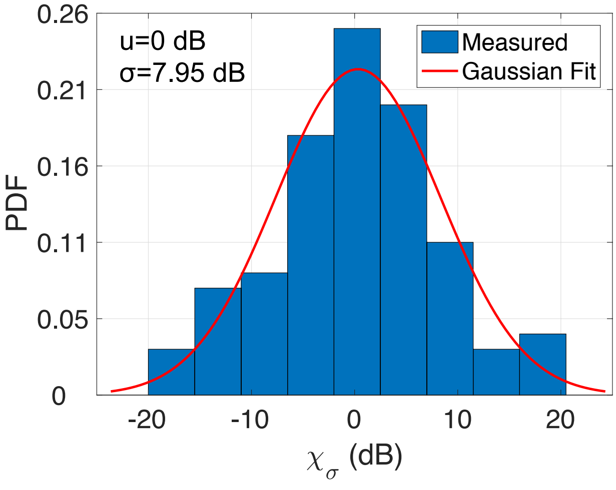

FIGURE 22. PDF of the cluster shadowing gain (X_σ) derived from the clustering model.

TABLE 4. Maximum Deviation (D_v) Values Between the Cluster Shadowing Gain/Number of Rays and Distribution Fits

Distribution	D_v	
	Cluster Shadowing	**Number of Ray**
Rayleigh	0.720	0.177
Log-normal	0.057	0.184
Exponential	0.347	0.201
Nakagami	0.261	0.220
Normal	0.326	0.231
Rician	0.717	0.190
Weibull	0.062	0.193

Our empirical results of PDPs measured from all the measured positions show that the number of clusters N_{cluster} can be modeled as $N_{\text{cluster}} = N_{\min} + X$, where $N_{\min} = 1$ is the minimum number of clusters, and X is a Poisson distributed random variable with an average rate (λ) of 1.64. As a result, the mean of N_{cluster} is 2.64, which explains why 3 clusters are used in the proposed model, as summarized in the ninth row in Table 3. The CDF of the number of clusters from all the measured positions is presented in Fig. 23 to confirm the Poisson distribution. On the other hand, the number of rays within clusters can be modeled as Rayleigh distributed random variable with a mean value of 4.41, which explains why 4 rays are used in the proposed model, as summarized in the last row in Table 3. The mean value (μ) of the number of rays within clusters is estimated from the scale factor (σ_R) of the Rayleigh distribution [56], where $\mu = \sigma_R\sqrt{\pi/2}$. The CDF of the number of rays within clusters from all measured positions is presented in Fig. 24 and is modeled to be Rayleigh distributed. Several typical theoretical distributions have been tested, and the results are shown in the third column in Table 4. The Rayleigh distribution is observed to have the smallest D_v of 0.177 among all the tested distributions.

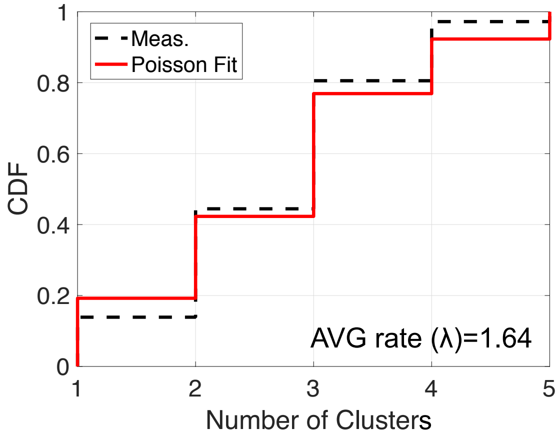

FIGURE 23. CDF of the number of clusters derived from the clustering model.

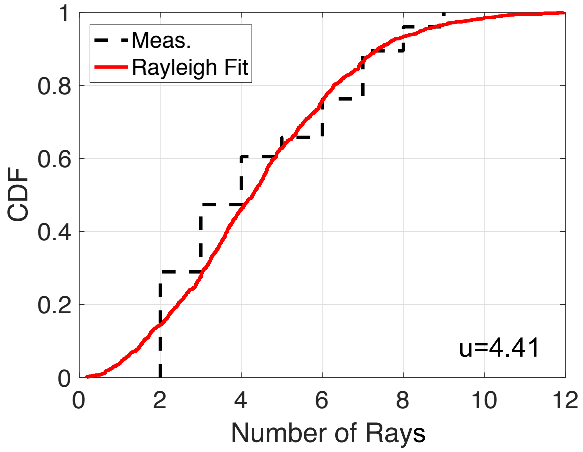

FIGURE 24. CDF of the number of rays derived from the clustering model.

A correlation coefficient matrix of parameters such as cluster power, cluster shadowing, τ_m, and τ_{rms}, is shown in Fig. 25. It can be observed that there are high correlations between cluster power and cluster shadowing, and between τ_m and τ_{rms}, respectively.

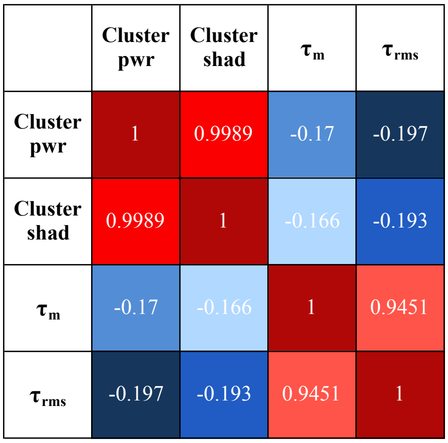

	Cluster pwr	**Cluster shad**	τ_m	τ_{rms}
Cluster pwr	1	0.9989	-0.17	-0.197
Cluster shad	0.9989	1	-0.166	-0.193
τ_m	-0.17	-0.166	1	0.9451
τ_{rms}	-0.197	-0.193	0.9451	1

FIGURE 25. Correlation coefficient matrix of parameters derived from the clustering model: cluster power, cluster shadowing, τ_m, and τ_{rms}.

4) Model Validation

The proposed clustering model is validated by comparing the distributions of the τ_{rms} derived from our model to that obtained from the measured data. The τ_{rms} is chosen because it is a standard criterion for validation of clustering models, and has been used in various publications such as [27], [28], [36]. To derive the τ_{rms} from the proposed model, we first synthesize the PDP using the parameters presented in Table 3, then estimate the τ_{rms} from the synthesized PDP using (2). Two examples of the measured (red solid line) and synthesized/modeled (black dash line) PDPs in the OLoS links with cables serving as obstruction with different Tx/Rx (horizontal) positions have been presented in Figs. 26 (a) and (b). It can be observed that the modeled PDPs have a good agreement with the measurements and that the dominant MPCs above the threshold are clearly captured by the model.

Figure 27 presents the CDF of the modeled τ_{rms} and the measured τ_{rms} obtained from all the measured positions. Vi-

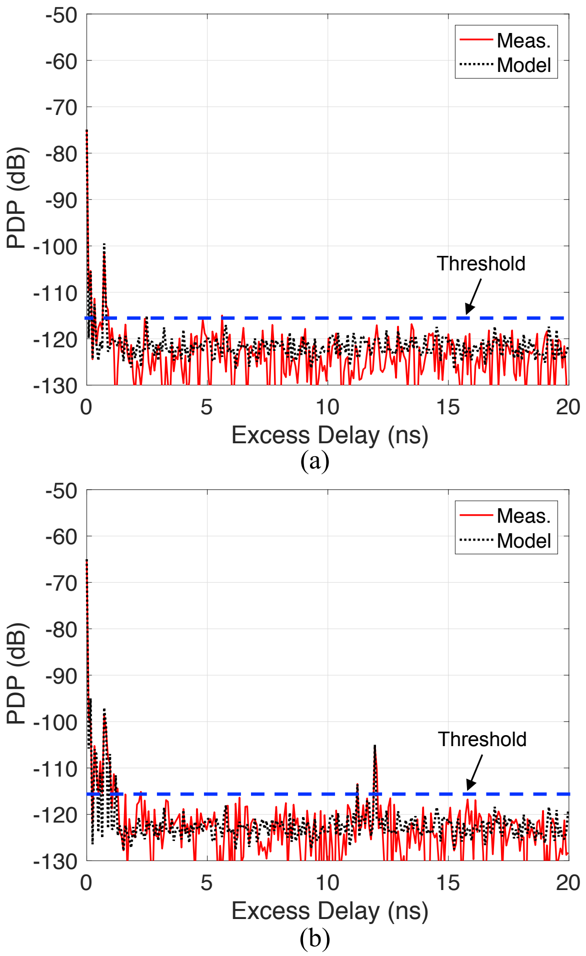

(a)

(b)

FIGURE 26. Comparison of the measured (red solid line) and modeled (black dash line) PDPs in the OLoS link with cables serving as obstruction, where (a) and (b) present the results from two different Tx/Rx (horizontal) positions.

sually, we have observed that the distribution of the modeled τ_{rms} is in good agreement with the measured data, where the μ and σ are estimated as -95.06 dB and 3.17 dB, respectively. In addition to the visual inspection, a maximum deviation value metric [54], $D_v = \text{Max}|F_{\text{model}}(\text{x}) - F_{\text{measurement}}(\text{x})|$, where $F_{\text{model}}(\text{x})$ and $F_{\text{measurement}}(\text{x})$ are the distributions obtained from the model and measurements, respectively, is used to quantify the fitness of the model with respect to the measured data. The value of D_v is estimated as 0.153, which is small according to [55] and thus confirms a good fit. Please note that the statistics of the clustering model are derived from the number of measurement points collected in this measurement campaign. To acquire a more generalized statistical characterization of the clustering model, complementary measurements in other data centers with multiple Tx/Rx positions would be required to validate how much the model parameters change from data center to data center. This is, however, a challenge often encountered in channel modeling, especially for a data center environment, where special permission is required to access the facility since data centers hold sensitive or proprietary information. Nonetheless, the measurement designs and results provided in this paper are the starting point for realistic performance evaluations and designs of THz communication systems in a data center environment.

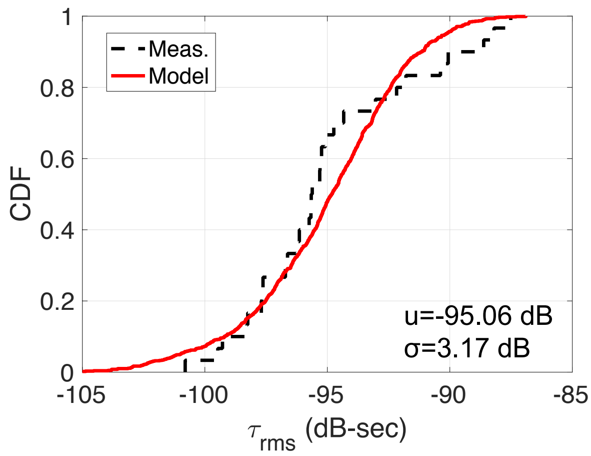

FIGURE 27. CDF of the measured and modeled τ_{rms} obtained from all the measured positions in the OLoS, NLoS, and ONLoS links.

IV. CONCLUSION

A THz channel measurement campaign conducted in a data center environment and its corresponding results have been presented. Various propagation scenarios such as LoS, NLoS, OLoS, and ONLoS links have been studied. Channel properties such as pathloss, PDP, and delay spread have been analyzed. We found that optical lenses can provide additional gain of 29.3 dB in the LoS link at d = 175 cm, and 12.6 dB in the NLoS link at a path length of 282 cm, respectively. We also found that cables and mesh structure can cause additional attenuation of about 20 dB and 6 dB, respectively. Existing objects in data centers, e.g., server-rack frames/pillars, serve as ideal reflectors for the NLoS type of link. Furthermore, the Tx/Rx misalignment tolerance range is found to approximate the diameter of the lens, and the impact of cooling airflow on THz propagation can be overlooked. Finally, a cluster-based propagation model for THz propagation in a data center environment has been proposed and validated with measured data, where the average numbers of clusters and rays are estimated as 3 and 4, respectively, and the average inter-arrival time of clusters $(1/\Lambda)$ and rays $(1/\lambda)$ are estimated as 4.4 ns and 0.24 ns, respectively.

ACKNOWLEDGEMENT

The authors would like to thank Prof. Ada Gavrilovska and Yogendra Joshi for their kind permission to conduct measurements in the data center at the Tech Way Building. They would also like to thank James Tyson and Mitchell Baxendale for their help with preparing the data center. This work has been financially supported, in part, by National Science Foundation grant 1651273.

REFERENCES

[1] S. Mollahasani and E. Onur, "Evaluation of Terahertz Channel in Data Centers," in NOMS 2016 - 2016 IEEE/IFIP Network Operations and Management Symposium, Apr. 2016, pp. 727–730.

[2] S. Rommel, T. R. Raddo, and I. T. Monroy, "Data Center Connectivity by 6G Wireless Systems," in 2018 Photonics in Switching and Computing (PSC), Sep. 2018, pp. 1–3.

[3] K. Ramachandran, R. Kokku, R. Mahindra, and S. Rangarajan, "60 GHz Data-Center Networking: Wireless = Worry Less?" in NEC Technical Report, Jul. 2008.

[4] D. Halperin, S. Kandula, J. Padhye, P. Bahl, and D. Wetherall, "Augmenting Data Center Networks with Multi-Gigabit Wireless Links," SIGCOMM Comput. Commun. Rev., vol. 41, no. 4, pp. 38–49, Aug. 2011.

[5] T. Chen, X. Gao, and G. Chen, "The Features, Hardware, and Architectures of Data Center Networks: A Survey," Journal of Parallel and Distributed Computing, vol. 96, pp. 45–74, Oct. 2016.

[6] Y. Cui, H. Wang, X. Cheng, and B. Chen, "Wireless Data Center Networking," IEEE Wireless Communications, vol. 18, no. 6, pp. 46–53, Dec. 2011.

[7] X. Zhou, Z. Zhang, Y. Zhu, Y. Li, S. Kumar, A. Vahdat, B. Y. Zhao, and H. Zheng, "Mirror Mirror on the Ceiling: Flexible Wireless Links for Data Centers," in Proceedings of the ACM SIGCOMM Conference on Applications, Technologies, Architectures, and Protocols for Computer Communication, ser. SIGCOMM '12. New York, NY, USA: ACM, Aug. 2012, pp. 443–454.

[8] A. S. Hamza, J. S. Deogun, and D. R. Alexander, "Wireless Communication in Data Centers: A Survey," IEEE Communications Surveys Tutorials, vol. 18, no. 3, pp. 1572–1595, 2016.

[9] Gigazine. (2008) Compare Cables That Are Tangled Together and Cables Organized Beautifully Like Art. [Online]. Available: https://gigazine.net/gsc_news/en/20081020_dirty_clean_cable/

[10] A. Davy, L. Pessoa, C. Renaud, E. Wasige, M. Naftaly, T. Kürner, G. George, O. Cojocari, N. O. Mahony, and M. A. G. Porcel, "Building An End User Focused THz Based Ultra High Bandwidth Wireless Access Network: the TERAPOD Approach," in 9th International Congress on Ultra Modern Telecommunications and Control Systems and Workshops (ICUMT), Nov. 2017, pp. 454–459.

[11] V. Petrov, J. Kokkoniemi, D. Moltchanov, J. J. Lehtomäki, Y. Koucheryavy, and M. J. Juntti, "Last Meter Indoor Terahertz Wireless Access: Performance Insights and Implementation Roadmap," IEEE Communications Magazine, vol. 56, no. 6, pp. 158–165, Jun. 2018.

[12] B. Peng and T. Kürner, "A Stochastic Channel Model for Future Wireless THz Data Centers," in International Symposium on Wireless Communication Systems (ISWCS), Aug. 2015, pp. 741–745.

[13] N. Boujnah, S. Ghafoor, and A. Davy, "Modeling and Link Quality Assessment of THz Network Within Data Center," in 2019 European Conference on Networks and Communications (EuCNC), Jun. 2019, pp. 57–62.

[14] J. M. Eckhardt, T. Doeker, S. Rey, and T. Kürner, "Measurements in a Real Data Centre at 300 GHz and Recent Results," in 2019 13th European Conference on Antennas and Propagation (EuCAP), Mar. 2019, pp. 1–5.

[15] T. Kürner, G. M. Ke, A. F. Molisch, A. Bo, H. Ruisi, L. Guangkai, T. Li, D. Jianwu, and Z. Zhangdui, "Millimeter Wave and THz Propagation Channel Modeling for High-Data Rate Railway Connectivity—Status and Open Challenges," in ZTE Commun., vol. 14, no. S1, Dec. 2016.

[16] S. Kim and A. Zajić, "Characterization of 300-GHz Wireless Channel on a Computer Motherboard," IEEE Transactions on Antennas and Propagation, vol. 64, no. 12, pp. 5411–5423, Dec. 2016.

[17] S. Kim and A. Zajić, "Statistical Characterization of 300-GHz Propagation on a Desktop," IEEE Transactions on Vehicular Technology, vol. 64, no. 8, pp. 3330–3338, Aug 2015.

[18] S. Kim and A. Zajić, "Statistical Modeling and Simulation of Short-Range Device-to-Device Communication Channels at Sub-THz Frequencies," IEEE Transactions on Wireless Communications, vol. 15, no. 9, pp. 6423–6433, Sept 2016.

[19] C.-L. Cheng, S. Kim, and A. Zajić, "Comparison of Path Loss Models for Indoor 30 GHz, 140 GHz, and 300 GHz Channels," in 11th European Conference on Antennas and Propagation (EUCAP), Mar. 2017, pp. 716–720.

[20] J. Fu, P. Juyal, and A. Zajić, "300 GHz Channel Characterization of Chip-to-Chip Communication in Metal Enclosure," in 2019 13th European Conference on Antennas and Propagation (EuCAP), Mar. 2019, pp. 1–5.

[21] "IEEE Standard for High Data Rate Wireless Multi-Media Networks–Amendment 2: 100 Gb/s Wireless Switched Point-to-Point Physical Layer," IEEE Std 802.15.3d-2017 (Amendment to IEEE Std 802.15.3-2016 as amended by IEEE Std 802.15.3e-2017), pp. 1–55, Oct. 2017.

[22] C.-L. Cheng and A. Zajić, "Characterization of 300 GHz Wireless Channels for Rack-to-Rack Communications in Data Centers," in 2018 IEEE 29th Annual International Symposium on Personal, Indoor, and Mobile Radio Communications (PIMRC), Sep. 2018.

[23] C.-L. Cheng, S. Sangodoyin, and A. Zajić, "THz MIMO Channel Characterization for Wireless Data Center-Like Environment," in 2019 IEEE International Symposium on Antennas and Propagation USNC/URSI National Radio Science Meeting, Jul. 2019.

[24] C.-L. Cheng and A. Zajić, "Characterization of Propagation Phenomena Relevant for 300 GHz Wireless Data Center Links," IEEE Transactions on Antennas and Propagation, (accepted).

[25] C.-L. Cheng, S. Sangodoyin, and A. Zajić, "Terahertz MIMO Fading Analysis and Doppler Modeling in a Data Center Environment," in 14th European Conference on Antennas and Propagation (EUCAP), (submitted).

[26] A. A. M. Saleh and R. Valenzuela, "A Statistical Model for Indoor Multipath Propagation," IEEE Journal on Selected Areas in Communications, vol. 5, no. 2, pp. 128–137, Feb. 1987.

[27] S. Sangodoyin, V. Kristem, A. F. Molisch, R. He, F. Tufvesson, and H. M. Behairy, "Statistical Modeling of Ultrawideband MIMO Propagation Channel in A Warehouse Environment," IEEE Transactions on Antennas and Propagation, vol. 64, no. 9, pp. 4049–4063, Sep. 2016.

[28] S. Sangodoyin, V. Kristem, C. U. Bas, M. Käske, J. Lee, C. Schneider, G. Sommerkorn, C. J. Zhang, R. Thomä, and A. F. Molisch, "Cluster Characterization of 3-D MIMO Propagation Channel in an Urban Macrocellular Environment," IEEE Transactions on Wireless Communications, vol. 17, no. 8, pp. 5076–5091, Aug. 2018.

[29] F. Fuschini, S. Häfner, M. Zoli, R. Müller, E. M. Vitucci, D. Dupleich, M. Barbiroli, J. Luo, E. Schulz, V. Degli-Esposti, and R. S. Thomä, "Analysis of In-Room mm-Wave Propagation: Directional Channel Measurements and Ray Tracing Simulations," Journal of Infrared, Millimeter, and Terahertz Waves, vol. 38, no. 6, pp. 727–744, Jun. 2017.

[30] S. Salous, V. Degli Esposti, F. Fuschini, D. Dupleich, R. Müller, R. S. Thomä, K. Haneda, J.-M. Molina Garcia-Pardo, J. Pascual Garcia, D. P. Gaillot, M. Nekovee, and S. Hur, "Millimeter-Wave Propagation: Characterization and Modeling Toward Fifth-Generation Systems. [Wireless Corner]," IEEE Antennas and Propagation Magazine, vol. 58, no. 6, pp. 115–127, Dec. 2016.

[31] C. Gustafson, K. Haneda, S. Wyne, and F. Tufvesson, "On mm-Wave Multipath Clustering and Channel Modeling," IEEE Transactions on Antennas and Propagation, vol. 62, no. 3, pp. 1445–1455, Mar. 2014.

[32] N. Iqbal, J. Luo, R. Müller, G. Steinböck, C. Schneider, D. A. Dupleich, S. Häfner, and R. S. Thomä, "Multipath Cluster Fading Statistics and Modeling in Millimeter-Wave Radio Channels," IEEE Transactions on Antennas and Propagation, vol. 67, no. 4, pp. 2622–2632, Apr. 2019.

[33] S. Priebe, M. Jacob, and T. Kürner, "AoA, AoD and ToA Characteristics of Scattered Multipath Clusters for THz Indoor Channel Modeling," in 17th European Wireless 2011 - Sustainable Wireless Technologies, Apr. 2011, pp. 1–9.

[34] S. Priebe and M. Jacob and T. Kürner, "Angular and RMS Delay Spread Modeling in View of THz Indoor Communication Systems," Radio Science, vol. 49, no. 3, pp. 242–251, Mar. 2014.

[35] Y. Choi, "Performances and Feasibility of THz Indoor Communication for Multi-Gigabit Transmission," in 2013 1st International Conference on Artificial Intelligence, Modelling and Simulation, Dec. 2013, pp. 446–450.

[36] H. Asplund, A. A. Glazunov, A. F. Molisch, K. I. Pedersen, and M. Steinbauer, "The COST 259 Directional Channel Model-Part II: Macrocells," IEEE Transactions on Wireless Communications, vol. 5, no. 12, pp. 3434–3450, Dec. 2006.

[37] Custom Transmitters, Virginia Diodes, Inc., Charlottesville, VA, USA. [Online]. Available: http://vadiodes.com/en/products/custom-transmitters

[38] Phase Locked Dielectric Resonator Oscillators, Ultra Electronics, Herley, Lancaster, PA, USA. [Online]. Available: https://www.ultra-herley.com/uploads/herley/datasheets/cti/Ultra%20Herley%20Series%20PDRO.pdf

[39] Frequency Multiplier - 33 to 50 GHz, Norden Millimeter, Placerville, CA, USA. [Online]. Available: https://www.nordengroup.com/product-group/frequency-multiplier-33-to-50-ghz/

[40] Multipliers - VDI Model: WR6.5x3, Virginia Diodes, Inc., Charlottesville, VA, USA. [Online]. Available: https://www.vadiodes.com/en/frequency-multipliers/10-products/165-wr65x3

[41] Mixers - VDI Model: WR2.8SHM, Virginia Diodes, Inc., Charlottesville, VA, USA. [Online]. Available: https://www.vadiodes.com/index.php/en/12-product/126-wr28shm12

[42] Nominal Horn Specifications, Virginia Diodes, Inc., Charlottesville, VA, USA. [Online]. Available: https://vadiodes.com/VDI/pdf/VDI%20Feedhorn%20Summary%202006_05.pdf

[43] Plano-Convex PTFE Lens, Thorlabs, Inc., Newton, NJ, USA. [Online]. Available: https://www.thorlabs.com/thorproduct.cfm?partnumber=LAT075

[44] 1U, 2U, 3U, 4U, 5U, 6U, and 7U, Nov. 2018. [Online]. Available: https://www.computerhope.com/jargon/num/1u.htm

[45] W. Zhang, X. Zhou, L. Yang, Z. Zhang, B. Y. Zhao, and H. Zheng, "3D Beamforming for Wireless Data Centers," in Proceedings of the 10th ACM Workshop on Hot Topics in Networks, ser. HotNets-X. New York, NY, USA: ACM, Nov. 2011, pp. 4:1–4:6.

[46] C. Zhang, F. Wu, X. Gao, and G. Chen, "Free Talk in the Air: A Hierarchical Topology for 60 GHz Wireless Data Center Networks," IEEE/ACM Transactions on Networking, vol. 25, no. 6, pp. 3723–3737, Dec. 2017.

[47] J. M. Jornet and I. F. Akyildiz, "Channel Modeling and Capacity Analysis for Electromagnetic Wireless Nanonetworks in the Terahertz Band," IEEE Transactions on Wireless Communications, vol. 10, no. 10, pp. 3211–3221, Oct. 2011.

[48] S. R. Saunders, Antennas & Propagation for Wireless Communications. USA: John Wiley & Sons, Inc., 2004.

[49] N. Czink, P. Cera, J. Salo, E. Bonek, J. Nuutinen, and J. Ylitalo, "A Framework for Automatic Clustering of Parametric MIMO Channel Data Including Path Powers," in IEEE Vehicular Technology Conference, Sep. 2006, pp. 1–5.

[50] M. Toeltsch, J. Laurila, K. Kalliola, A. F. Molisch, P. Vainikainen, and E. Bonek, "Statistical Characterization of Urban Spatial Radio Channels," IEEE Journal on Selected Areas in Communications, vol. 20, no. 3, pp. 539–549, Apr. 2002.

[51] A. F. Molisch, J. R. Foerster, and M. Pendergrass, "Channel Models for Ultrawideband Personal Area Networks," IEEE Wireless Communications, vol. 10, no. 6, pp. 14–21, Dec. 2003.

[52] J. Karedal, S. Wyne, P. Almers, F. Tufvesson, and A. F. Molisch, "A Measurement-Based Statistical Model for Industrial Ultra-Wideband Channels," IEEE Transactions on Wireless Communications, vol. 6, no. 8, pp. 3028–3037, Aug. 2007.

[53] Y. Ai, M. Cheffena, and Q. Li, "Power Delay Profile Analysis and Modeling of Industrial Indoor Channels," in 2015 9th European Conference on Antennas and Propagation (EuCAP), Apr. 2015, pp. 1–5.

[54] S. M. Ross, Simulation. New York, NY, USA: Academic, 2013.

[55] S. Sangodoyin and A. F. Molisch, "Impact of Body Mass Index on Ultrawideband MIMO BAN Channels-Measurements and Statistical Model," IEEE Transactions on Wireless Communications, vol. 17, no. 9, pp. 6067–6081, Sep. 2018.

[56] Wikipedia. Rayleigh Distribution. [Online]. Available: https://en.wikipedia.org/wiki/Rayleigh_distribution

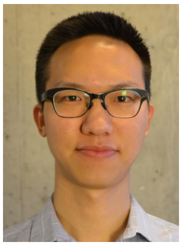

CHIA-LIN CHENG (S'17) received the B.Sc. degree in electrical engineering from the National Taiwan University in 2013 and the M.Sc. degree in electrical engineering from the Georgia Institute of Technology in 2017, respectively. He is currently pursuing his PhD in the Electromagnetic Measurements in Communications and Computing (EMC^2) Lab at the Georgia Institute of Technology focusing on mm-wave and THz wireless channel measurements and modeling. His research interests span areas of electromagnetics, wireless channel measurements and modeling. He was the recipient of the TechConnect Innovation Award (2019) and the Best Poster Award at the IEEE International Conference on RFID (2018).

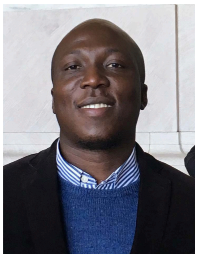

SEUN SANGODOYIN received the B.Sc. degree in electrical engineering from Oklahoma State University, Stillwater, OK, USA, in May 2007, and the M.Sc. and Ph.D. degrees in electrical engineering from the University of Southern California, Los Angeles, CA, USA, in 2009 and 2018, respectively. He is currently a Postdoctoral Fellow with the Georgia Institute of Technology, Atlanta, GA, USA. His research interests include millimeter-wave (measurement-based) MIMO channel modeling and analysis, terahertz communications, UWB MIMO radar, parameter estimation, body-area networks, and stochastic dynamical systems.

ALENKA ZAJIĆ (S'99-M'09-SM'13) received the B.Sc. and M.Sc. degrees form the School of Electrical Engineering, University of Belgrade, in 2001 and 2003, respectively. She received her Ph.D. degree in Electrical and Computer Engineering from the Georgia Institute of Technology in 2008. Currently, she is an Associate Professor in the School of Electrical and Computer Engineering at Georgia Institute of Technology. Prior to that, she was a visiting faculty member in the School of Computer Science at Georgia Institute of Technology, a post-doctoral fellow in the Naval Research Laboratory, and a design engineer at Skyworks Solutions Inc. Her research interests span areas of electromagnetic, wireless communications, signal processing, and computer engineering. Dr. Zajić was the recipient of the 2017 NSF CAREER award, the Best Paper Award at MICRO 2016, 2012 Neal Shepherd Memorial Best Propagation Paper Award, the Best Student Paper Award at the IEEE International Conference on Communications and Electronics 2014, the Best Paper Award at the International Conference on Telecommunications 2008, the Best Student Paper Award at the 2007 Wireless Communications and Networking Conference, and the Dan Noble Fellowship in 2004, which was awarded by Motorola Inc. and the IEEE Vehicular Technology Society for quality impact in the area of vehicular technology.